catalysts

MDPI

Article

Electrocatalytic Oxygen Reduction to Hydrogen Peroxide on Graphdiyne-Based Single-Atom Catalysts: First-Principles Studies

Kangkang Lian [1], Qiang Wan [1], Rong Jiang [2,*] and Sen Lin [1,*]

[1] State Key Laboratory of Photocatalysis on Energy and Environment, College of Chemistry, Fuzhou University, Fuzhou 350002, China
[2] Institute of Advanced Energy Materials, College of Chemistry, Fuzhou University, Fuzhou 350002, China
* Correspondence: jiangrong@fzu.edu.cn (R.J.); slin@fzu.edu.cn (S.L.)

Abstract: The electrocatalytic oxygen reduction reaction ($2e^-$ ORR) via a two-electron process is a promising pathway for the production of hydrogen peroxide (H_2O_2). Here, we systematically investigated the $2e^-$ ORR process on graphdiyne (GDY) supported single transition metal atoms (TM_1@GDY) using density functional theory (DFT) calculations. Among the 23 TM_1@GDY catalysts, Pt_1@GDY showed the best performance for the H_2O_2 product with an overpotential as low as 0.15 V. The electronic structure analysis, on the one hand, elucidates that the electron transfer between Pt_1@GDY and the adsorbed O_2 facilitates the activation of O_2, and, on the other hand, reveals that the high $2e^-$ ORR activity of Pt_1@GDY lies in the transfer of electrons from the filled Pt-3d orbitals to the 2p antibonding orbitals of OOH*, which effectively activates the O–O bond. This work provides insights to design efficient electrocatalysts for H_2O_2 generation.

Keywords: ORR; density functional theory (DFT); graphdiyne (GDY); electrocatalytic; single-atom catalysts; H_2O_2

Citation: Lian, K.; Wan, Q.; Jiang, R.; Lin, S. Electrocatalytic Oxygen Reduction to Hydrogen Peroxide on Graphdiyne-Based Single-Atom Catalysts: First-Principles Studies. *Catalysts* **2023**, *13*, 307. https://doi.org/10.3390/catal13020307

Academic Editor: C. Heath Turner

Received: 8 January 2023
Revised: 21 January 2023
Accepted: 26 January 2023
Published: 30 January 2023

1. Introduction

Hydrogen peroxide (H_2O_2) is an important green chemical with various applications in industrial processes such as paper bleaching, textiles, water treatment [1–4] and chemical synthesis [5]. More importantly, COVID-19, which is currently sweeping the world, has intensified the demand for H_2O_2 for medical purposes. Global production of H_2O_2 was close to 4.5 million tons in 2020, and the market demand is expected to reach approximately 5.7 million tons by 2027 [6]. However, current industrial H_2O_2 production relies mainly on the anthraquinone oxidation (AO) process, which is costly and highly polluting [7]. In addition, transporting, storing and handling high concentrations of H_2O_2 is dangerous and expensive. Hence, it has become urgent to develop a simple, low-cost and environmentally friendly method for H_2O_2 production. In recent years, electrocatalytic reduction of O_2 has been considered as a promising method for the production of H_2O_2 [8–10]. In this case, H_2O_2 can be produced on-site, which is both safe and convenient. The electrocatalytic O_2 reduction reaction (ORR) involves multiple electron steps, where O_2 can be reduced to H_2O_2 via the $2e^-$ pathway or to H_2O via the $4e^-$ route. Therefore, the main challenge in H_2O_2 production with the electrocatalytic ORR is how to control the selectivity of the reaction.

An increasing number of catalysts for the electrocatalytic synthesis of H_2O_2 have been reported recently, including noble metal [11,12] and their alloy catalysts [9,13,14], single-atom catalysts and carbon-based catalysts [15–17]. Among these, carbon-based catalysts are of great interest due to their abundant sources and easy tunability. In particular, graphene-based single-atom catalysts (SACs) have been designed and applied for the preparation of H_2O_2. For example, previous studies have reported that metal–nitrogen–carbon SACs can promote the selectivity of the electrocatalytic $2e^-$ ORR while

maintaining high activity [18–20]. As a member of the carbon material family, graphdiyne (GDY) has recently been reported in various fields [21]. Importantly, single metal atoms can be stably anchored on the GDY surface [22,23] due to the in-plane conjugated network of alkyl and aryl groups and the inhomogeneous charge distribution of GDY. More importantly, the pristine GDY monolayer (Figure 1a) has an excellent electron mobility, reaching 10^5 $cm^2/(Vs)$ at 300 K [24]. These advantages of GDY make it of great potential as a substrate for electrocatalysts.

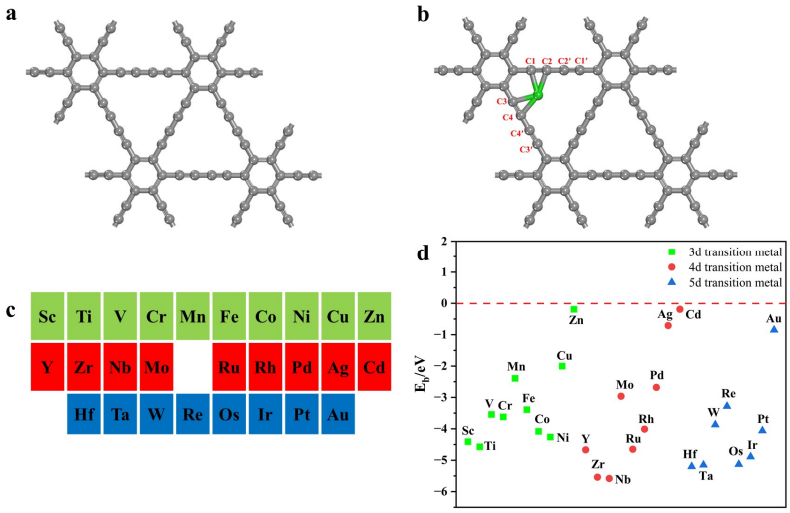

Figure 1. (**a**) Structure of GDY monolayer. (**b**) Structure of TM_1@GDY single-atom catalyst with different C sites labeled. Gray represents C atoms while green represents transition metal atoms. (**c**) The transition metal atoms investigated in this work. (**d**) Calculated binding energy (E_b) of TM_1 over different TM_1@GDY.

In this work, we have investigated the activity of a series of single transition metal atoms (TM_1) supported on GDY (TM_1@GDY) for the $2e^-$ ORR using density functional theory (DFT) calculations under acidic conditions (pH = 0). Of all the TM_1@GDYs, calculations showed that Pt_1@GDY has the best activity and selectivity in the $2e^-$ ORR. Encouragingly, the predicted activity of Pt_1@GDY is comparable to that of known commercial catalysts. Electronic structure analysis further revealed the origin of the high activity of Pt_1@GDY towards the $2e^-$ ORR. This work provides insight into the design of efficient electrocatalysts for the production of H_2O_2.

2. Results and Discussion

2.1. Catalyst Structure and Stability

As the stability of a catalyst is a prerequisite for its application, we first assessed the thermal stability of TM_1@GDY by calculating the binding energy (E_b) of TM_1 on GDY. As shown in Figure 1b, TM_1 prefers to adsorb on corners near the six-membered carbon ring and is bonded to four carbon atoms. TM_1 involves all 3d, 4d and 5d transition metal elements except for radioactive technetium (Tc), lanthanides (La~Lu) and the liquid metal mercury (Hg), as shown in Figure 1c. The E_b of TM_1 was calculated as follows:

$$E_b = E_{TM_1@GDY} - E_{TM_1} - E_{GDY} \quad (1)$$

where $E_{TM_1@GDY}$ and E_{GDY} represent the total energy of TM_1@GDY and GDY, respectively, and E_{TM_1} represents the energy of the single transition metal atom. The E_b of all TM_1@GDY are shown in Figure 1d and Table S1 from Supplementary Materials, and the $E_b < 0$ indicated that the single metal atom can be stably supported on GDY. It is found that the E_b of single atoms of zinc (Zn), cadmium (Cd), argentum (Ag) and aurum (Au) are less than 0 eV but greater than −1 eV. Their optimized structures are shown in Figure S1 from Supplementary

Materials. However, it is found that the Zn and Cd on GDY are not at the corners of the acetylene ring but at the center of the ring. They are far from the GDY plane at distances of 2.32 and 3.03 Å, respectively, indicating that Cd_1@GDY and Zn_1@GDY are unstable. The E_b of both Ag_1 and Au_1@GDY are very close to 0 eV, indicating that they are also unstable. Meanwhile, the E_b of Cu_1@GDY was calculated to be −2.00 eV. Notably, Li et al. synthesized Cu single atoms anchored to GDY and demonstrated that the supported Cu_1 is very stable [25]. Therefore, we consider the supported single atoms with E_b more negative than −2.00 eV to be stable by using Cu_1@GDY as a criterion. Accordingly, Zn, Cd, Ag and Au single atoms are relatively unstable because their E_b is more positive than −2.00 eV.

2.2. Catalyst Performance

The ORR performance of TM_1@GDY under acidic conditions (pH = 0) was investigated. The scheme of the reaction process is shown in Figure 2a. Firstly, the adsorbed O_2 on TM_1@GDY obtained one (electron (e^-) and proton (H^+)) pair from the aqueous solution, producing an OOH* intermediate. Followed by the further reduction of OOH* by ($H^+ + e^-$), this step can generate either H_2O_2 ($2e^-$ ORR) or H_2O ($4e^-$ ORR), and the product depends on if the O–O bond is broken. The steps of the ORR are as follows, the * in the following steps represents the adsorption site on the catalyst [26]:

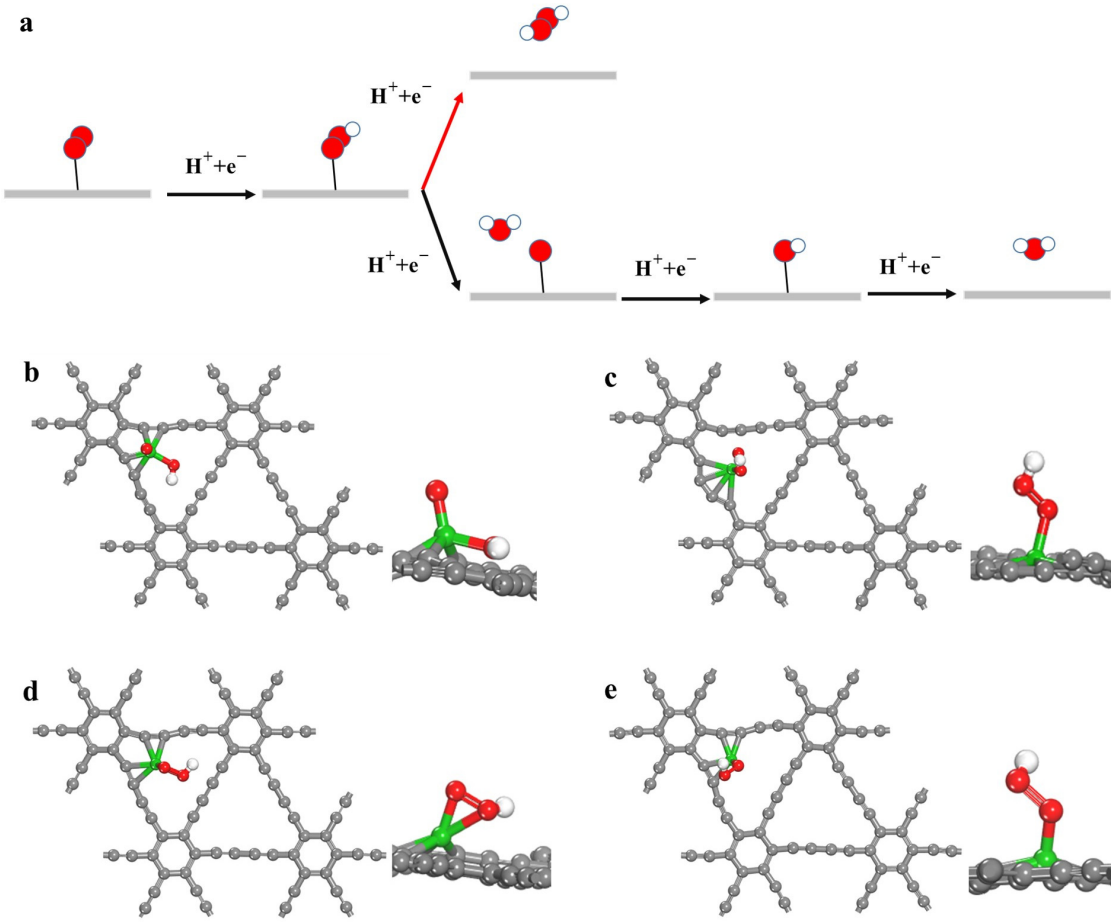

Figure 2. (**a**) Scheme of the $2e^-$ ORR and $4e^-$ ORR pathways. Different adsorption types of intermediate OOH: (**b**) O–O bond cleavage after OOH adsorption to form a *(O + OH) intermediate on TM_1@GDY (TM = Re, W, Nb, Ta and Mo), (**c**) after OOH adsorption, a single atom is transferred to the acetylene chain on TM_1@GDY (TM = Sc, Y and Hf), (**d**) side-on adsorption pattern of OOH on TM_1@GDY (TM = Ti, V, Mn, Zr, Rh and Ir), and (**e**) end-on adsorption mode of OOH on TM_1@GDY (TM = Pt, Pd, Cu, Co, Ni, Ru, Os, Cr and Fe). Color scheme: H: White; C: Gray; O: Red; Transition metals (TM): Green.

The $2e^-$ ORR pathway:

$$O_2 + * + H^+ + e^- \rightarrow OOH* \quad (2)$$

$$OOH* + H^+ + e^- \rightarrow H_2O_2 + * \quad (3)$$

The complete reaction can be expressed as:

$$O_2 + 2H^+ + 2e^- \rightarrow H_2O_2 \ (0.7 \text{ V vs. SHE}) \quad (4)$$

The $4e^-$ ORR pathway:

$$O_2 + * + H^+ + e^- \rightarrow OOH* \quad (5)$$

$$OOH* + H^+ + e^- \rightarrow H_2O + O* \quad (6)$$

$$O* + H^+ + e^- \rightarrow OH* \quad (7)$$

$$OH* + H^+ + e^- \rightarrow H_2O + * \quad (8)$$

The complete reaction can be expressed as:

$$O_2 + 4H^+ + 4e^- \rightarrow 2H_2O \ (1.23 \text{ V vs. SHE}) \quad (9)$$

From the above ORR reaction pathway, it is clear that the $4e^-$ ORR and $2e^-$ ORR are two competing reactions during the electrochemical synthesis of H_2O_2, which depends on the type of O_2 adsorption [26]. The adsorption of O_2 on the catalyst surface can be generally classified into two types: end-on and side-on modes [27]. Obviously, in both the $4e^-$ and $2e^-$ pathways, the intermediate OOH* is formed in the first step of oxygen adsorption and hydrogenation, so we first calculated the free energy of OOH* (G_{OOH*}) (Table S2 from Supplementary Materials). As shown in Equations (5) and (6), the ΔG of each electron step in the $2e^-$ ORR under ideal conditions is 0.70 eV (G_{OOH*} = 4.22 eV), so the change in free energy of the whole reaction is 1.40 eV ($G_{H_2O_2}$ = 3.52 eV).

In general, the adsorption conformations of OOH* on these TM_1@GDYs can be divided into four types, as shown in Figure 2b–e. The first one (TM = Re, W, Nb, Ta and Mo) is shown in Figure 2b, where the O–O bond of OOH* undergoes spontaneous cleavage due to strong interactions between OOH* and TM_1@GDY, indicating the poor selectivity of these TM_1@GDYs (TM = Re, W, Nb, Ta and Mo). For the second one shown in Figure 2c (TM = Sc, Y and Hf), the G_{OOH*} of OOH* are all less than 3.52 eV (Table S1 from Supplementary Materials), which indicates that Sc_1, Y_1 and Hf_1@GDY have strong adsorption of OOH. In addition, after OOH adsorption, a facile migration of the single atom to the C–C triple bond site (located between C2 and C2′) can be observed, indicating that the single atom is unstable during the catalysis. In the third one (TM = Ti, V, Mn, Zr, Rh and Ir), OOH* is in the side-on mode (Figure 2d); it can be seen that the G_{OOH*} of the laterally adsorbed OOH* are all less than 3.52 eV (Table S1), which means that ΔG_{OOH*} are greater than 1.40 eV, which is not favorable for the $2e^-$ ORR. For the last one (TM = Pt, Pd, Cu, Co, Ni, Ru, Os, Cr and Fe, Figure 2e), OOH* is following the end-on pattern. The G_{OOH*} are all greater than 3.52 eV, which means that these TM_1@GDYs have strong adsorption of OOH, and is, therefore, favorable for the $2e^-$ ORR pathway. Therefore, the structures in Figure 2e were used for the subsequent studies.

Next, we compared the electrocatalytic ORR performance of TM_1@GDYs (TM = Pt, Pd, Cu, Co, Ni, Ru, Os, Cr and Fe). The free energy curves, as well as the corresponding η and potential limiting steps, are given in Figure 3 and Figure S2 from Supplementary Materials to further clarify the catalytic activity and selectivity. We can see that the G_{OOH*} on Cr_1@GDY, Fe_1@GDY, Co_1@GDY, Cu_1@GDY, Ru_1@GDY and Os_1@GDY are 2.53 eV, 3.15 eV, 3.44 eV, 3.50 eV, 2.41 eV and 2.55 eV, respectively (Figure S2 from Supplementary Materials and Figure 3a,c), which are all lower than 3.52 eV, implying that they all have a strong adsorption for OOH*. Therefore, this strong adsorption of OOH* leads to the second

elementary step of the 2e$^-$ ORR being uphill and becoming PDS. In contrast, the G_{OOH*} of the other three catalysts (Ni_1@GDY, Pd_1@GDY and Pt_1@GDY) are 3.76 eV, 4.41 eV and 4.07 eV, respectively (Figure 3b,d–f), which are all above 3.52 eV. In particular, the G_{OOH*} of Pd_1@GDY and Pt_1@GDY (4.41 eV and 4.07 eV) are very close to 4.22 eV, which indicates that the adsorption strength of OOH is moderate on both catalysts with the first and second elementary step as PDS, respectively. In contrast, the G_{OOH*} of Ni_1@GDY is lower than 4.22 eV, which indicates a stronger adsorption of OOH*, leading to the second step as PDS and thus unfavorable to the 2e$^-$ ORR pathway.

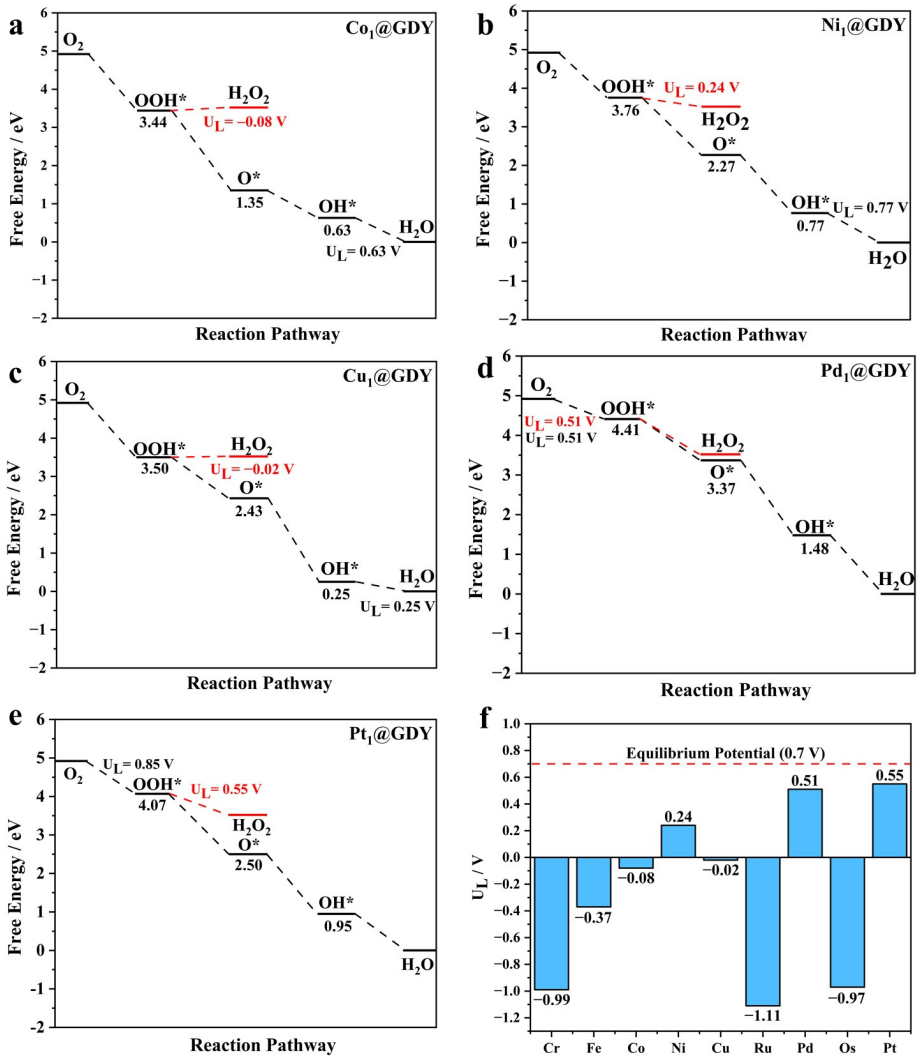

Figure 3. Free energy diagrams of the 2e$^-$ and 4e$^-$ ORR on (**a**) Co_1@GDY, (**b**) Ni_1@GDY, (**c**) Cu_1@GDY, (**d**) Pd_1@GDY and (**e**) Pt_1@GDY. Red curve: the 2e$^-$ ORR pathway. Black curve: the 4e$^-$ ORR pathway. The potential-determining step (PDS) of the 2e$^-$ and 4e$^-$ ORR on Co_1@GDY, Ni_1@GDY and Cu_1@GDY is the second and fourth step, respectively. The PDSs of the 2e$^-$ and 4e$^-$ ORR on Pd_1@GDY are the first step. The PDSs of the 2e$^-$ and 4e$^-$ ORR on Pt_1@GDY are the second and first step, respectively. (**f**) Limiting potential (U_L) of the 2e$^-$ ORR on TM_1@GDY (TM = Co, Ni, Cu, Pd, and Pt) catalysts. The red dashed line represents the equilibrium potential which is equal to 0.70 V.

In addition, we can see the 4e$^-$ ORR pathway on each TM_1@GDY in Figure 3 and Figure S2 from Supplementary Materials. The PDSs of Cr_1@GDY, Fe_1@GDY, Ru_1@GDY and Os_1@GDY are the fourth step (Figure S2 from Supplementary Materials), which are all uphill in energy with ΔG equal to 0.90 eV, 0.23 eV, 0.72 eV and 0.94 eV, respectively. This suggests that the 4e$^-$ ORR process cannot be spontaneous. As can be seen from

Figure 3a–c, the PDS of Co_1@GDY, Ni_1@GDY and Cu_1@GDY is the last reaction step with ΔG of −0.63 eV, −0.77 eV and −0.25 eV, respectively, while the PDS of the 4e⁻ ORR on Pd_1@GDY and Pt_1@GDY (Figure 3d,e) is the first reaction step with ΔG of −0.51 eV and −0.85 eV, respectively.

For the 2e⁻ ORR pathway, it is well known that a good catalyst for the electrochemical generation of H_2O_2 should have a U_L close to $U_{equilibrium}$. Therefore, U_L can be used as a descriptor to evaluate its 2e⁻ ORR activity. To better understand the ORR ability of catalysts, we calculated the U_L of the 2e⁻ and 4e⁻ ORR for these nine catalysts (Cr_1@GDY, Fe_1@GDY, Co_1@GDY, Ni_1@GDY, Cu_1@GDY, Ru_1@GDY, Pd_1@GDY, Os_1@GDY and Pt_1@GDY) by using the U_L formula and plotted Figure 3f and Figure S3 from Supplementary Materials with the red dashed lines representing the standard $U_{equilibrium}$, which are 0.7 V and 1.23 V, respectively. Theoretically, the closer the U_L is to $U_{equilibrium}$, the closer the G_{OOH^*} is to 4.22 eV, implying a higher 2e⁻ ORR activity of the catalyst. The reason is that G_{OOH^*} is lower than 3.52 eV when $U_L < 0$, i.e., the adsorption of OOH is too strong. In addition, η can be used more intuitively to evaluate the activity because $\eta = U_{equilibrium} - U_L$. It can be seen from Figure 3f that the catalysts with $U_L > 0$ are favorable catalysts for the 2e⁻ ORR. The results show that the U_L values of Ni_1@GDY, Pd_1@GDY and Pt_1@GDY are 0.24 V, 0.51V, and 0.55 V, corresponding to η of 0.46 V, 0.19 V, and 0.15 V, respectively. As a result, Pt_1@GDY and Pd_1@GDY have the smallest and second smallest η, which are comparable to those on Au(100) and Au(111) [28] and PtHg4 electrocatalysts [29], indicating that they have good 2e⁻ ORR activity.

In the ORR process, selectivity is a key indicator to evaluate the catalytic performance of the catalyst for H_2O_2 synthesis. Figure 4 shows the Gibbs free energy diagrams of the 2e⁻ and 4e⁻ ORRs on Pt_1@GDY. At U = 0 V (black curve), the reaction steps in both the 2e⁻ and 4e⁻ ORR proceed spontaneously, as their ΔG are negative. The results also show that ΔG_{PDS} is 0.55 eV for the 2e⁻ ORR and 0.85 eV for the 4e⁻ ORR. Thus, for the 2e⁻ ORR and 4e⁻ ORR, the free energy of the PDS changes to zero when the applied potential is equal to 0.55 V (blue curve) and 0.85 V (red curve), respectively, while the other steps remain downhill in energy. The PDS steps of both the 2e⁻ and 4e⁻ ORR are uphill when the applied potential is equal to $U_{equilibrium}$. The results also show that η is 0.15 V and 0.38 V for the 2e⁻ and 4e⁻ ORR, respectively, indicating that the 2e⁻ ORR exhibits higher selectivity over the 4e⁻ ORR on Pt_1@GDY. In conclusion, it is predicted that Pt_1@GDY is an ideal catalyst for the catalytic synthesis of H_2O_2.

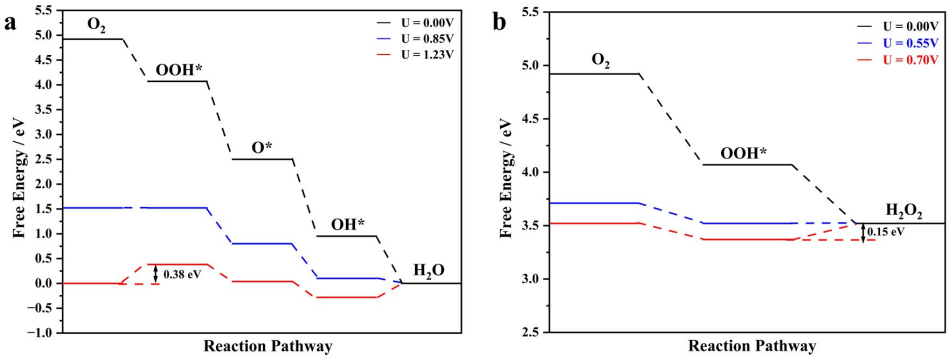

Figure 4. Free energy changes in the (**a**) 4e⁻ ORR and (**b**) 2e⁻ ORR on Pt_1@GDY with different voltages.

2.3. Origin of the 2e⁻ ORR Activity

Essentially, catalytic properties, such as activity, stability and selectivity, are often determined by the electronic structure of the catalyst [30]. Previously, we discussed in detail the effect of catalyst structure on the activity and selectivity of the 2e⁻ ORR. In order to better design catalysts for the 2e⁻ ORR, we further discussed the origin of catalytic activity using electronic structure analysis. First, we calculated the Bader charge and charge differential density (CDD). As shown in Figure 5a, the CDD results show that there is

significant electron transfer between Pt_1 and C atoms of Pt_1@GDY. From the Bader charge analysis, we find that about 0.32 e^- are transferred from Pt_1 to the C atom of GDY. This indicates that the interaction between Pt_1 and the C atoms allows Pt_1 to be stabilized on the GDY support. In addition, the CDD plot (Figure 5b) shows a significant charge transfer between Pt1 and OOH when OOH species are adsorbed on Pt_1@GDY. This leads to an elongation of the O–O bond length of OOH from 1.21 Å to 1.45 Å (Figure S4 from Supplementary Materials). Moreover, the Bader charge analysis further confirms that there is about 0.39 e^- transferred from Pt_1 to the adsorbed OOH. This implies that the Pt single atom effectively activates the O–O bond, which facilitates the subsequent hydrogenation of OOH* to generate the final H_2O_2 product.

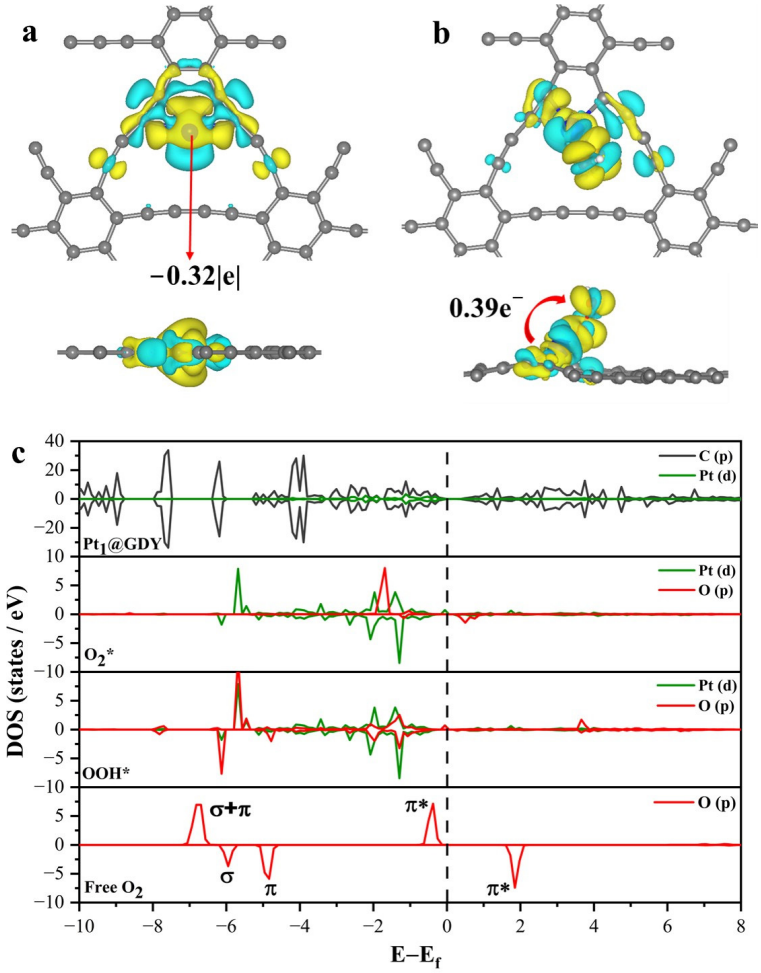

Figure 5. Top and side views of charge differential density (CDD) plots of (**a**) Pt_1@GDY and (**b**) OOH* on Pt_1@GDY. The blue and yellow areas represent positive and negative charge accumulation, respectively. The isosurface value is set to 0.002 e/Bohr^3. (**c**) Partial density of states (PDOSs) of the free O_2 and O_2*/OOH* on Pt_1@GDY. The Fermi level is set to zero.

Finally, we determined the activation mechanism of the O_2 molecule from the perspective of molecular orbital theory. First, as shown in Figure 5c, the obvious orbital overlap between Pt_1 3d and C 2p indicates a strong interaction between the anchored Pt1 and the surrounding C atoms, which further demonstrates the stability of Pt_1@GDY. Second, we investigated spin-polarized PDOSs to elucidate the interactions between Pt_1 and O atoms in O_2* and OOH* species. It is seen from Figure 5c that the 2p antibonding orbital π^* and the bonding orbital π of the free O_2 are near the Fermi level, which indicates that they are the most active orbitals of O_2. When the free O_2 is adsorbed onto Pt_1@GDY, the π^* antibonding orbitals of O_2 orbitals shift to the lower energy region and hybridize with the d orbitals of

Pt_1. On the other hand, the empty π* of O_2* is partially occupied, which indicates that the d electrons of Pt_1 are partially transferred to the empty π* of O_2, allowing O_2 to be activated. As shown in the PDOS diagram for OOH*, the 3d orbital of Pt_1 couples simultaneously with the bonding and antibonding orbitals of 2p of O, which leads to a moderate activation of the O–O bond in OOH. Thus, the electronic structure analysis suggests that the ORR process on Pt_1@GDY tends to follow the $2e^-$ pathway.

3. Materials and Methods

Computational Details

All spin-polarized DFT calculations were performed using the Vienna Ab-initio Simulation Packages (VASP.5.4.4) [31], and the electron–ion interaction was described with the projector-augmented wave (PAW) method [32,33]. The exchange-correlation potential was treated by the Perdew–Burke–Ernzerhof (PBE) version of the generalized gradient approximation (GGA) [34]. The valence electrons were expanded in a plane-wave basis set with an energy cutoff of 450 eV. The optimized monolayer GDY has a lattice constant of 18.74 Å (Figure 1a). The 2 × 2 supercells of GDY were adopted for the subsequent calculations. A 15 Å vacuum space was adopted along the z-direction to avoid interactions between periodic slabs. K-points mesh was set to 3 × 3 × 1 for Brillouin zone sampling in structural optimization and electronic structure calculations. The DFT-D3 method with zero-damping [35] was introduced to describe van der Waals weakly dispersive interactions (vdW). All the structures were relaxed until the forces on each ion were less than 0.05 eV/Å, and the convergence criteria for the energy was set as 10^{-4} eV.

Based on Nørskov's computational hydrogen electrode model [36,37], we calculated the Gibbs free energy change (ΔG) for each elementary step as follows:

$$\Delta G = \Delta E + \Delta E_{zpe} - T\Delta S + eU \quad (10)$$

where ΔE refers to the energy difference directly calculated with DFT before and after each elementary reaction step; ΔE_{zpe} and TΔS are the differences in the zero-point energies and entropies at 298.15 K, respectively; and the value of eU was determined using the applied potential (U).

In addition, we defined a descriptor of limiting potential (U_L) to describe the activity of the electrocatalytic ORR with the free energy change of the potential-determining step (PDS):

$$U_L = -\Delta G_{PDS}/e \quad (11)$$

where the ΔG_{PDS} is the Gibbs free energy change of PDS.

The overpotential (η) was calculated as:

$$\eta = U_{equilibrium} - U_L \quad (12)$$

where the equilibrium potentials ($U_{equilibrium}$) are 1.23 V and 0.70 V for the $4e^-$ ORR and $2e^-$ ORR, respectively.

4. Conclusions

In summary: the $2e^-$ ORR catalyzed by the GDY-supported single transition metal atom catalysts in an acidic environment was investigated using first-principles DFT calculations. The results show that Pt_1@GDY has good stability and the best activity for the $2e^-$ ORR, as it exhibits the lowest thermodynamic η (0.15 V) among the 23 catalysts studied. In addition, the electronic structure analysis of the interactions between O_2*, OOH* and Pt_1@GDY provides an in-depth understanding of the $2e^-$ ORR pathway to produce H_2O_2. The high activity of Pt_1@GDY is attributed to the electron transfer between the 3d orbital of Pt_1 and the antibonding orbital π* of the 2p orbital of O in OOH*, allowing the efficient activation of the O–O bond. This work provides theoretical insights into the design of efficient electrocatalysts for the generation of H_2O_2.

Supplementary Materials: The following supporting information can be downloaded at: https://www.mdpi.com/xxx/s1, Figure S1: Top and side views of the (**a**) Zn atom, (**b**) Cd atom, (**c**) Ag atom and (**d**) Au atom supported on GDY. Color scheme: C: Gray; Zn: Pink; Cd: Purple; Ag: Blue; Au: Yellow; Figure S2: Free energy diagrams of $2e^-$ and $4e^-$ ORR on (**a**): Fe_1@GDY; (**b**): Cr_1@GDY; (**c**): Ru_1@GDY; (**d**): Os_1@GDY; Figure S3: Limiting potentials of $4e^-$ ORR on TM_1@GDY (TM = Cr, Fe, Co, Ni, Cu, Ru, Pd, Os, and Pt) catalysts. The red line represents the equilibrium potential of $4e^-$ ORR.; Figure S4: The adsorption structure of OOH* on Pt_1@GDY and the O–O bond length; Table S1: The E_b on TM_1@GDY; Table S2: The G_{OOH^*} on TM_1@GDY.

Author Contributions: Conceptualization, R.J. and S.L.; methodology, K.L. and Q.W.; software, K.L. and Q.W.; validation, Q.W., R.J. and S.L.; formal analysis, K.L.; investigation, K.L.; resources, S.L.; data curation, K.L.; writing—original draft preparation, K.L.; writing—review and editing, K.L., Q.W., R.J. and S.L.; visualization, K.L.; supervision, S.L.; project administration, S.L.; funding acquisition, S.L. All authors have read and agreed to the published version of the manuscript.

Funding: Funds from the National Natural Science Foundation of China (21973013) and the National Natural Science Foundation of Fujian Province, China (2020J02025) are acknowledged. S.L. thanks the "Chuying Program" for the Top Young Talents of Fujian Province. DFT computations were performed at the Hefei advanced computing center and Supercomputing Center of Fujian.

Data Availability Statement: The datasets used to support the findings are included within the paper and in the Supplementary Materials.

Conflicts of Interest: The authors declare no conflict of interest.

References

1. Melchionna, M.; Fornasiero, P.; Prato, M. The Rise of Hydrogen Peroxide as the Main Product by Metal-Free Catalysis in Oxygen Reductions. *Adv. Mater.* **2019**, *31*, e1802920. [CrossRef]
2. Rozendal, R.A.; Leone, E.; Keller, J.; Rabaey, K. Efficient hydrogen peroxide generation from organic matter in a bioelectrochemical system. *Electrochem. Commun.* **2009**, *11*, 1752–1755. [CrossRef]
3. Kosaka, K.; Yamada, H.; Shishida, K.; Echigo, S.; Minear, R.A.; Tsuno, H.; Matsui, S. Evaluation of the treatment performance of a multistage ozone/hydrogen peroxide process by decomposition by-products. *Water Res.* **2001**, *35*, 3587–3594. [CrossRef]
4. Yamanaka, I.; Murayama, T. Neutral H2O2 synthesis by electrolysis of water and O2. *Angew. Chem. Int. Ed. Engl.* **2008**, *47*, 1900–1902. [CrossRef]
5. Ksibi, M. Chemical oxidation with hydrogen peroxide for domestic wastewater treatment. *Chem. Eng. J.* **2006**, *119*, 161–165. [CrossRef]
6. Zhang, X.L.; Su, X.; Zheng, Y.R.; Hu, S.J.; Shi, L.; Gao, F.Y.; Yang, P.P.; Niu, Z.Z.; Wu, Z.Z.; Qin, S.; et al. Strongly Coupled Cobalt Diselenide Monolayers for Selective Electrocatalytic Oxygen Reduction to H2O2 under Acidic Conditions. *Angew. Chem. Int. Ed. Engl.* **2021**, *60*, 26922–26931. [CrossRef]
7. Campos-Martin, J.M.; Blanco-Brieva, G.; Fierro, J.L. Hydrogen peroxide synthesis: An outlook beyond the anthraquinone process. *Angew. Chem. Int. Ed. Engl.* **2006**, *45*, 6962–6984. [CrossRef]
8. Jirkovsky, J.S.; Panas, I.; Ahlberg, E.; Halasa, M.; Romani, S.; Schiffrin, D.J. Single atom hot-spots at Au-Pd nanoalloys for electrocatalytic H2O2 production. *J. Am. Chem. Soc.* **2011**, *133*, 19432–19441. [CrossRef]
9. Zheng, Z.; Ng, Y.H.; Wang, D.W.; Amal, R. Epitaxial Growth of Au-Pt-Ni Nanorods for Direct High Selectivity H2O2 Production. *Adv. Mater.* **2016**, *28*, 9949–9955. [CrossRef]
10. Jiang, Y.; Ni, P.; Chen, C.; Lu, Y.; Yang, P.; Kong, B.; Fisher, A.; Wang, X. Selective Electrochemical H2O2 Production through Two-Electron Oxygen Electrochemistry. *Adv. Energy Mater.* **2018**, *8*, 1801909. [CrossRef]
11. Gervasini, A.; Carniti, P.; Desmedt, F.; Miquel, P. Liquid Phase Direct Synthesis of H2O2: Activity and Selectivity of Pd-Dispersed Phase on Acidic Niobia-Silica Supports. *ACS Catal.* **2017**, *7*, 4741–4752. [CrossRef]
12. Arrigo, R.; Schuster, M.E.; Abate, S.; Giorgianni, G.; Centi, G.; Perathoner, S.; Wrabetz, S.; Pfeifer, V.; Antonietti, M.; Schlögl, R. Pd Supported on Carbon Nitride Boosts the Direct Hydrogen Peroxide Synthesis. *ACS Catal.* **2016**, *6*, 6959–6966. [CrossRef]
13. Edwards, J.K.; Ntainjua, E.; Carley, A.F.; Herzing, A.A.; Kiely, C.J.; Hutchings, G.J. Direct synthesis of H_2O_2 from H_2 and O_2 over gold, palladium, and gold-palladium catalysts supported on acid-pretreated TiO_2. *Angew. Chem. Int. Ed. Engl.* **2009**, *48*, 8512–8515. [CrossRef]
14. Li, F.; Shao, Q.; Hu, M.; Chen, Y.; Huang, X. Hollow Pd–Sn Nanocrystals for Efficient Direct H2O2 Synthesis: The Critical Role of Sn on Structure Evolution and Catalytic Performance. *ACS Catal.* **2018**, *8*, 3418–3423. [CrossRef]
15. Sun, Y.; Sinev, I.; Ju, W.; Bergmann, A.; Dresp, S.; Kühl, S.; Spöri, C.; Schmies, H.; Wang, H.; Bernsmeier, D.; et al. Efficient Electrochemical Hydrogen Peroxide Production from Molecular Oxygen on Nitrogen-Doped Mesoporous Carbon Catalysts. *ACS Catal.* **2018**, *8*, 2844–2856. [CrossRef]

16. Han, L.; Sun, Y.; Li, S.; Cheng, C.; Halbig, C.E.; Feicht, P.; Hübner, J.L.; Strasser, P.; Eigler, S. In-Plane Carbon Lattice-Defect Regulating Electrochemical Oxygen Reduction to Hydrogen Peroxide Production over Nitrogen-Doped Graphene. *ACS Catal.* **2019**, *9*, 1283–1288. [CrossRef]
17. Iglesias, D.; Giuliani, A.; Melchionna, M.; Marchesan, S.; Criado, A.; Nasi, L.; Bevilacqua, M.; Tavagnacco, C.; Vizza, F.; Prato, M.; et al. N-Doped Graphitized Carbon Nanohorns as a Forefront Electrocatalyst in Highly Selective O_2 Reduction to H_2O_2. *Chem* **2018**, *4*, 106–123. [CrossRef]
18. Sun, Y.; Silvioli, L.; Sahraie, N.R.; Ju, W.; Li, J.; Zitolo, A.; Li, S.; Bagger, A.; Arnarson, L.; Wang, X.; et al. Activity-Selectivity Trends in the Electrochemical Production of Hydrogen Peroxide over Single-Site Metal-Nitrogen-Carbon Catalysts. *J. Am. Chem. Soc.* **2019**, *141*, 12372–12381. [CrossRef]
19. Gao, J.; Yang, H.B.; Huang, X.; Hung, S.-F.; Cai, W.; Jia, C.; Miao, S.; Chen, H.M.; Yang, X.; Huang, Y.; et al. Enabling Direct H_2O_2 Production in Acidic Media through Rational Design of Transition Metal Single Atom Catalyst. *Chem* **2020**, *6*, 658–674. [CrossRef]
20. Li, B.Q.; Zhao, C.X.; Liu, J.N.; Zhang, Q. Electrosynthesis of Hydrogen Peroxide Synergistically Catalyzed by Atomic Co-Nx-C Sites and Oxygen Functional Groups in Noble-Metal-Free Electrocatalysts. *Adv. Mater.* **2019**, *31*, e1808173. [CrossRef]
21. Li, Y.; Xu, L.; Liu, H.; Li, Y. Graphdiyne and graphyne: From theoretical predictions to practical construction. *Chem. Soc. Rev.* **2014**, *43*, 2572–2586. [CrossRef]
22. Jiao, Y.; Du, A.; Hankel, M.; Zhu, Z.; Rudolph, V.; Smith, S.C. Graphdiyne: A versatile nanomaterial for electronics and hydrogen purification. *Chem. Commun.* **2011**, *47*, 11843–11845. [CrossRef]
23. He, J.; Ma, S.Y.; Zhou, P.; Zhang, C.X.; He, C.; Sun, L.Z. Magnetic Properties of Single Transition-Metal Atom Absorbed Graphdiyne and Graphyne Sheet from DFT+U Calculations. *J. Phys. Chem. C* **2012**, *116*, 26313–26321. [CrossRef]
24. He, T.; Matta, S.K.; Will, G.; Du, A. Transition-Metal Single Atoms Anchored on Graphdiyne as High-Efficiency Electrocatalysts for Water Splitting and Oxygen Reduction. *Small Methods* **2019**, *3*, 1800419. [CrossRef]
25. Yu, J.; Cao, C.; Jin, H.; Chen, W.; Shen, Q.; Li, P.; Zheng, L.; He, F.; Song, W.; Li, Y. Uniform single atomic Cu1-C4 sites anchored in graphdiyne for hydroxylation of benzene to phenol. *Natl. Sci. Rev.* **2022**, *9*, nwac018. [CrossRef]
26. Kulkarni, A.; Siahrostami, S.; Patel, A.; Norskov, J.K. Understanding Catalytic Activity Trends in the Oxygen Reduction Reaction. *Chem. Rev.* **2018**, *118*, 2302–2312. [CrossRef]
27. Ye, C.-W.; Xu, L. Recent advances in the design of a high performance metal–nitrogen–carbon catalyst for the oxygen reduction reaction. *J. Mater. Chem. A* **2021**, *9*, 22218–22247. [CrossRef]
28. Viswanathan, V.; Hansen, H.A.; Rossmeisl, J.; Norskov, J.K. Unifying the 2e- and 4e- Reduction of Oxygen on Metal Surfaces. *J. Phys. Chem. Lett.* **2012**, *3*, 2948–2951. [CrossRef]
29. Siahrostami, S.; Verdaguer-Casadevall, A.; Karamad, M.; Deiana, D.; Malacrida, P.; Wickman, B.; Escudero-Escribano, M.; Paoli, E.A.; Frydendal, R.; Hansen, T.W.; et al. Enabling direct H2O2 production through rational electrocatalyst design. *Nat. Mater.* **2013**, *12*, 1137–1143. [CrossRef]
30. Pan, J.; Fang, Q.; Xia, Q.; Hu, A.; Sun, F.; Zhang, W.; Yu, Y.; Zhuang, G.; Jiang, J.; Wang, J. Dual effect of the coordination field and sulphuric acid on the properties of a single-atom catalyst in the electrosynthesis of H2O2. *Phys. Chem. Chem. Phys.* **2021**, *23*, 21338–21349. [CrossRef]
31. Kresse, G.; Hafner, J. Ab initio molecular dynamics for liquid metals. *Phys. Rev. B* **1993**, *47*, 558–561. [CrossRef]
32. Kresse, G.; Joubert, D. From ultrasoft pseudopotentials to the projector augmented-wave method. *Phys. Rev. B* **1999**, *59*, 1758–1775. [CrossRef]
33. Blochl, P.E. Projector augmented-wave method. *Phys. Rev. B* **1994**, *50*, 17953–17979. [CrossRef]
34. Perdew, J.P.; Burke, K.; Ernzerhof, M. Generalized Gradient Approximation Made Simple. *Phys. Rev. Lett.* **1996**, *77*, 3865–3868. [CrossRef] [PubMed]
35. Grimme, S.; Antony, J.; Ehrlich, S.; Krieg, H. A consistent and accurate ab initio parametrization of density functional dispersion correction (DFT-D) for the 94 elements H-Pu. *J. Chem. Phys.* **2010**, *132*, 154104. [CrossRef]
36. Nørskov, J.K.; Rossmeisl, J.; Logadottir, A.; Lindqvist, L.; Kitchin, J.R.; Bligaard, T.; Jónsson, H. Origin of the Overpotential for Oxygen Reduction at a Fuel-Cell Cathode. *J. Phys. Chem. B* **2004**, *108*, 17886–17892. [CrossRef]
37. Valdés, Á.; Qu, Z.W.; Kroes, G.J.; Rossmeisl, J.; Nørskov, J.K. Oxidation and Photo-Oxidation of Water on TiO2 Surface. *J. Phys. Chem. C* **2008**, *112*, 9872–9879. [CrossRef]